

The mutual influence of two buildings on their wind-driven rain exposure and comments on the obstruction factor

B. Blocken* ^(a), G. Dezsö ^(b), J. van Beeck ^(b), J. Carmeliet ^(c,d)

(a) Building Physics and Systems, Eindhoven University of Technology, P.O. box 513, 5600 MB Eindhoven, The Netherlands

(b) Department of Environmental and Applied Fluid Dynamics, von Karman Institute for Fluid Dynamics, Waterloosesteenweg 72, 1640 Sint-Genesius-Rode, Belgium

(c) Chair of Building Physics, Swiss Federal Institute of Technology ETHZ, ETH-Hönggerberg, CH-8093 Zürich, Switzerland

(d) Empa, Swiss Federal Laboratories for Materials Testing and Research, Laboratory for Building Technologies, Überlandstrasse 129, CH-8600 Dübendorf, Switzerland

Abstract

Wind-driven rain (WDR) deposition on a two-building configuration is studied with Computational Fluid Dynamics (CFD). The configuration consists of a high-rise building screened by a low-rise building. Validation of the wind-flow simulations is performed with Particle Image Velocimetry (PIV) measurements in a wind tunnel. Raindrop motion is simulated by Lagrangian particle tracking in the mean wind-flow pattern with a reference wind speed $U_{10} = 10$ m/s. Horizontal rainfall intensities $R_h = 5$ mm/h and 30 mm/h are considered. Simulations of WDR are performed for the two-building configuration and for each building separately, to analyse the mutual influence of the buildings on their WDR deposition pattern. The simulation results indicate that this influence is very pronounced and that it is to some extent opposite to what might be expected. The low-rise building influences the deposition on the high-rise building (downstream disturbance), not by partly shielding it from wind and WDR, but by increasing the strength of the standing vortex between the two buildings. This locally increases WDR intensities on the high-rise building facade by more than a factor 2 for both $R_h = 5$ mm/h and 30 mm/h. On the other hand, the high-rise building influences deposition on the low-rise building facade (upstream disturbance) by the wind-blocking effect. This effect yields a reduction in WDR deposition on the low-rise building facade by up to about 25% for both $R_h = 5$ and 30 mm/h. In the European Standard Draft for WDR assessment, the mutual influence can only be taken into account by a simplified reduction factor, called the obstruction factor. It only considers downstream disturbances, and does not consider the possibility of increased WDR deposition due to neighbouring buildings. Care should therefore be exercised when using the current version of the obstruction factor to determine WDR exposure.

Keywords: Wind-driven rain; Driving rain; Wind flow; Raindrop trajectories; Impact; Catch ratio; Building; Computational Fluid Dynamics (CFD); Numerical simulation; Validation

1. Introduction

The deposition of wind-driven rain (WDR) on buildings is of concern because it is one of the most important moisture sources affecting the hygrothermal behaviour and durability of building facades. Three categories of methods exist to assess the amount of WDR that is deposited on building facades: experimental, semi-empirical and numerical methods (Blocken and Carmeliet 2004). The introduction of numerical methods (Computational Fluid Dynamics; CFD) in WDR research has provided the capability to meticulously study the complex interaction between WDR and buildings. The CFD numerical simulation technique for WDR was developed by Choi (1991, 1993, 1994) and extended in the time domain by Blocken and Carmeliet (2002, 2007a). The steady-state simulation technique by Choi allows determining the spatial distribution of WDR on buildings under steady-state conditions of wind and rain, i.e. for fixed, static values of wind speed, wind direction and horizontal rainfall intensity (i.e. the rainfall intensity falling through a horizontal plane). This technique has been adopted by a large number of researchers for their WDR analyses. Validation studies of the steady-state simulation technique were performed by e.g. Hangan (1999) and van Mook (2002). The extension of this technique in the

* Corresponding author: Bert Blocken, Building Physics and Systems, Eindhoven University of Technology, P.O. box 513, 5600 MB Eindhoven, the Netherlands. Tel: +31 (0)40 247 2138, Fax: +31 (0)40 243 8595. *E-mail address:* b.j.e.blocken@tue.nl

time domain allowed the numerical determination of both the spatial and temporal distribution of WDR on buildings. Validation studies for a low-rise building and for different rain events have indicated that this extended numerical method can provide quite accurate predictions of the WDR amount and the WDR deposition pattern on the building facade (Blocken and Carmeliet 2002, 2006, 2007b). Recently, additional validation studies, based on the extended numerical method, were made for two rather complex high-rise buildings and for a simple rectangular test building, showing a satisfactory agreement between simulations and measurements (Tang and Davidson 2004, Abuku et al. 2009, Briggen et al. 2009). Abuku et al. (2009) specifically focused on validation for oblique wind directions.

In spite of the large amount of research work done in the past, there are important topics in CFD studies of WDR on buildings that have not yet or hardly been addressed. Two of these are mentioned here because they are part of this paper. (1) Up to now, almost all CFD WDR studies were conducted for isolated (single-standing) buildings. In reality however, buildings seldom stand alone. To the knowledge of the authors, there is only one publication in which a preliminary CFD study was made of WDR on a combination of two high-rise buildings (Karagiozis et al. 1997). More research on the influence of surrounding buildings on the WDR exposure of building facades is needed. (2) The CFD simulation technique allows a detailed determination of the spatial and temporal distribution of WDR on building facades. However, this technique is often too complex and time-consuming for practical WDR assessment. On the other hand, the semi-empirical European Standard Draft prEN ISO 15927-3 (CEN 2006) is fast and easy to use, but it cannot provide such detailed information. The mutual influence of buildings, for example, can only be taken into account by a simplified reduction factor, called the “obstruction factor”. The power of CFD can be used to study the accuracy of the European Standard Draft (ESD) procedure and, eventually, to provide some improvements to this procedure.

In this paper, CFD simulations of WDR on a two-building configuration are presented. The configuration consists of a high-rise building ($L_2 \times B_2 \times H_2 = 50 \times 12.5 \times 50 \text{ m}^3$) screened by a low-rise building ($L_1 \times B_1 \times H_1 = 50 \times 12.5 \times 12.5 \text{ m}^3$) (Fig. 1). The distance between both buildings is 25 m. Wind direction is perpendicular to the building facades. This particular configuration is chosen because it has been one of the common configurations studied in earlier work on building aerodynamics in which the interaction effect of both buildings on the flow pattern has been described (Wise et al. 1965, Sexton 1968, Wise 1970, Penwarden and Wise 1975). The mutual influence of the two buildings on their WDR exposure is investigated in the present paper by performing simulations, not only for the two-building configuration, but also for each building separately. The CFD results will also be used to discuss the performance of the ESD obstruction factor. In Section 2, the definitions and parameters of WDR are given. Section 3 briefly presents the numerical WDR model. In section 4, the model validation based on the wind tunnel measurements with Particle Image Velocimetry (PIV) is described. Section 5 presents and discusses the simulation results of WDR deposition on the facades. The ESD obstruction factor is discussed in section 6. Finally, sections 7 (discussion) and 8 (conclusions) conclude the paper.

2. Definitions and parameters

The quantities that are used to describe WDR are the specific catch ratio $\eta_d(d)$, related to the raindrop diameter d , and the catch ratio η , related to the entire spectrum of raindrop diameters:

$$\eta_d(d,t) = \frac{R_{\text{wdr}}(d,t)}{R_h(d,t)} ; \quad \eta(t) = \frac{R_{\text{wdr}}(t)}{R_h(t)} \quad (1)$$

where $R_{\text{wdr}}(d,t)$ and $R_h(d,t)$ are the specific WDR intensity on the building and the specific unobstructed horizontal rainfall intensity, and t is the time. $R_{\text{wdr}}(t)$ and $R_h(t)$ respectively refer to the same quantities but integrated over all raindrop diameters. The unobstructed horizontal rainfall intensity is the intensity of rainfall through a horizontal plane that is situated outside the wind-flow pattern that is disturbed by the building (i.e. the rainfall that would be measured by a rain gauge with a horizontal orifice at ground-level, placed in an open field).

The catch ratio η is a complicated function of space and time. The six basic influencing parameters for η are: (1) the building geometry (including environment topography), (2) the position on the building facade, (3) the reference wind speed, (4) the reference wind direction, (5) the horizontal rainfall intensity and (6) the horizontal raindrop-size distribution. The reference wind speed U_{10} (m/s) is usually taken as the horizontal component of the wind-velocity vector at 10 m height in the upstream undisturbed flow. The reference wind direction ϕ_{10} (degrees from north) refers to the direction of the reference wind speed. The horizontal raindrop-size distribution $f_h(d)$ (m^{-1}) refers to the raindrop-size distribution as a flux through a horizontal plane (Blocken and Carmeliet 2004). In reality, the turbulent dispersion of raindrops is an additional parameter. It is often neglected, as will be done in this paper. This decision is based on the findings by Choi (1997) and by Blocken and Carmeliet (2002) and on a review of the literature (Blocken and Carmeliet 2004).

3. Numerical wind-driven rain model

The numerical model for the simulation of WDR on buildings developed by Choi (1991, 1993, 1994) and extended by Blocken and Carmeliet (2002, 2007a) consists of the five steps mentioned below. For more information, the reader is referred to the literature.

1. The wind-flow pattern around the building is calculated using a CFD code. Usually the steady Reynolds-Averaged Navier-Stokes (RANS) equations are solved and a k - ϵ turbulence model is used to provide closure.
2. Raindrop trajectories are obtained by injecting raindrops of different sizes in the calculated wind-flow pattern and by solving their equations of motion (Lagrangian particle tracking).
3. The specific catch ratio (η_d) is determined from the configuration of the calculated raindrop trajectories using the “steady stream tube” approach. In a steady-state wind-flow pattern and ignoring turbulent dispersion of raindrops, three raindrop trajectories from a steady stream tube. The steady stream tube approach is based on mass conservation of the raindrops in this stream tube (see Choi 1994, Blocken and Carmeliet 2002), and allows to calculate η_d at a given position from only three computed raindrop trajectories.
4. The catch ratio is calculated from the specific catch ratio and from the horizontal raindrop-size distribution.
5. When the four previous steps are executed for several combinations of reference wind speed U_{10} , wind direction ϕ_{10} and horizontal rainfall intensity R_h , the obtained data can be used to construct catch-ratio charts for different zones (positions) at the building facade. Experimental data records of U_{10} , ϕ_{10} and R_h (10-minute values) can then be combined with these catch-ratio charts to determine the corresponding spatial and temporal distribution of WDR on the building facade.

In this paper, only steps 1 to 4 will be performed. Step 5 is mentioned here because it has been important in past validation studies of WDR simulations, as will be described next.

4. Model validation

4.1. Validation strategy

In the 5-step CFD simulation model for WDR, probably the most important modelling assumptions are embedded in the calculation of the wind-flow pattern with steady RANS and a turbulence model (step 1). The calculations in steps 2 to 5 are generally considered to be less critical although also some assumptions are made here that might require validation, e.g. neglecting the turbulent dispersion of raindrops. Validation of CFD simulations of WDR can be performed in two ways: (1) by comparing calculated and measured wind-flow patterns (result of step 1); and/or (2) by comparing calculated and measured WDR amounts (result of steps 1 to 4 in case of stationary wind and rain, or of steps 1 to 5 in case of real transient rain events). Previous validation studies of WDR used the second approach. This approach however is only feasible for the limited number of building configurations for which high-quality experimental WDR data are available, either from full-scale measurements (van Mook 2002, Tang et al. 2004, Blocken and Carmeliet 2005, Nore et al. 2007) or from wind tunnel experiments of WDR (Surry et al. 1994, Inculet and Surry 1994, Inculet 2001). For the present study that focuses on a specific two-building configuration, no experimental WDR data are available. Because validation is most important for the wind-flow pattern, a set of wind tunnel measurements with PIV was established.

4.2. Wind tunnel experiments

The experiments were conducted in the L-2B wind tunnel at the von Karman Institute for Fluid Dynamics. It is a low-speed, open-circuit wind tunnel of the suction type, with a $0.35 \times 0.35 \text{ m}^2$ test section. The measurements were conducted at a scale of 1:750, using 2D PIV. Two sets of mean wind speed and turbulence profiles were measured in the wind tunnel: (1) the “approach flow profiles”, with hot-wire anemometry, at a distance of 200 mm (150 m in full scale) upstream of the location where the buildings would be positioned; and (2) the “incident flow profiles”, with PIV, at the location where the buildings would be positioned. The measurements indicated differences between both sets of profiles, indicating a developing atmospheric boundary layer (ABL) in the tunnel. To avoid having to simulate a developing ABL with CFD – which is particularly difficult with steady RANS (Blocken et al. 2007a), the incident profiles will be used as inlet profiles for the CFD simulations, as will be explained in the next section. These profiles are given in Fig. 2. The wind speed profile closely resembles a logarithmic law with $u^* = 1.1 \text{ m/s}$ and $y_0 = 0.00125 \text{ m}$ ($\approx 1 \text{ m}$, full scale). The incident reference wind speed at height 0.1 m ($y/H_2 = 1.5$) is 11.5 m/s .

The building models were constructed from PMMA. The model-scale dimensions are $L_2 \times B_2 \times H_2 = 0.067 \times 0.017 \times 0.067 \text{ m}^3$ for the high-rise building, and $L_1 \times B_1 \times H_1 = 0.067 \times 0.017 \times 0.017 \text{ m}^3$ for the low-rise building, with a distance in between of 0.033 m . Measurements were made for three configurations: (1) the isolated low-rise building; (2) the isolated high-rise building; and (3) the two-building configuration. The wind

direction was perpendicular to the windward facades of the building models and the measurements were made in the vertical building centreplane. The maximum blockage ratio was 3.6%, and the minimum building Reynolds number was 11,500.

The PIV setup and image acquisition have been described in (Sagrado et al. 2002, Dezsö-Weidinger et al. 2003). The PIV system was made of the following components: A BMI Series 5000 Nd:YAG laser that can provide successive two pulses up to 400 mJ each. A pulse generator from Stanford Research Systems Inc. (model DG535) was used in connection with a camera of PCO Computer Optics GmbH (SensiCam CCD, S/N: 370LD0825, 1280/1024 pixels). Spherical and cylindrical lenses and a prism produced the laser sheet of 1.5 mm thickness and 200 mm wide. The camera was mounted with a 105/F2.5 Nikkor lens. Both cavities of the laser were shooting with maximum power. The images of the camera were recorded on a Personal Computer.

For the particle seeding of the flow, an oil droplets generator was used, generating droplets of ± 1 μm , thus small enough to follow the flow. The time delay between the two laser pulses was $\Delta t = 225$ μs . Recording of a series of 150 successive images took about 15 minutes. Averages were later calculated on these series. The post-processing of the PIV images to obtain the velocity fields was done by WIDIM, developed by Scarano and Riethmuller (2000). The measurement results will be presented in section 4.4 together with the CFD results.

4.3. Numerical simulations: characteristics and settings

3D steady RANS simulations are performed at model scale, in a computational domain with a maximum blockage ratio 1.4%. Note that the cross-section of this domain is larger than the wind tunnel cross-section. The reason is to allow simulations with oblique wind directions in the same domain, without having to rotate the building within the domain. The buildings are positioned at a distance $5H_2$ from the inlet plane and one of the side planes (Franke et al. 2007, Tominaga et al. 2008a). For each building configuration, hybrid grids are used. Figs. 3a-c display the grids at the building surfaces and at part of the bottom of the computational domain. These grids are a combination of a high-resolution structured hexahedral grid, for high grid quality near the building surfaces and in the passage, a low-resolution structured hexahedral grid from a certain distance from the building(s) to the side edges of the domain, and an unstructured wedge (prismatic) grid, for a grid-economical transition from the high-resolution to the low-resolution grid. For each building configuration, the grid resolution was determined by grid-sensitivity analyses on three grids with a refinement factor $\sqrt{2}$. The resulting grids had 67,557 cells for the isolated low-rise building, 80,664 cells for the isolated high-rise building and 199,593 cells for the two-building configuration.

The commercial CFD code Fluent 6.3.26 is used to solve the 3D RANS equations using the control volume method. Four different turbulence models are applied: (1) the standard k- ϵ model by Jones and Launder (1972); (2) the Renormalisation Group (RNG) k- ϵ model by Yakhot et al. (1992); (3) the realizable k- ϵ model by Shih et al. (1995); and (4) the Reynolds stress model (RSM) (Launder et al. 1975) with a linear pressure-strain model and wall-reflection effects (Gibson and Launder 1978, Launder 1989). The wall-reflection term ensures redistribution of the normal stresses near the wall. It tends to damp the normal stress perpendicular to the wall while enhancing the stresses parallel to the wall. The turbulence model equations can be found in the related references, the model constants used in this study are the default values in Fluent 6.3.26 (Fluent Inc. 2006):

- standard k- ϵ model: $C_{1\epsilon} = 1.44$; $C_{2\epsilon} = 1.92$; $C_\mu = 0.09$; $\sigma_k = 1.0$; $\sigma_\epsilon = 1.3$
- RNG k- ϵ model: $C_{1\epsilon} = 1.42$; $C_{2\epsilon} = 1.68$; $C_\mu = 0.0845$
- realizable k- ϵ model: $C_{1\epsilon} = 1.44$; $C_2 = 1.9$; $\sigma_k = 1.0$; $\sigma_\epsilon = 1.2$
- RSM with wall reflection effects: $C_{1\epsilon} = 1.44$; $C_{2\epsilon} = 1.92$; $C_\mu = 0.09$; $C_{1PS} = 1.8$; $C_{2PS} = 0.6$; $C_{1'PS} = 0.5$; $C_{2'PS} = 0.3$; $\sigma_k = 1$; $\sigma_\epsilon = 1.3$.

In the subscripts, PS refers to “pressure-strain”. Pressure-velocity coupling is taken care of by the SIMPLE algorithm. Pressure interpolation is second order. Second order discretization schemes are used for both the convection terms and the viscous terms of the governing equations.

The vertical inlet profiles of mean wind speed, turbulent kinetic energy and turbulence dissipation rate are obtained from the “incident flow” measurements. Turbulence intensity is converted to turbulent kinetic energy by assuming $\sigma_v \approx \sigma_w$. Turbulence dissipation rate $\epsilon = u_*^3/\kappa(y+y_0)$, where the von Karman constant $\kappa = 0.42$. The sides and the top of the computational domain are modelled as slip walls (zero normal velocity and zero normal gradients of all variables). At the outlet, zero static pressure is specified. At the building and ground surfaces, the standard wall functions by Launder and Spalding (1974) with equivalent sand-grain roughness (k_s) modifications according to the formulae by Cebeci and Bradshaw (1977) are used (k_s -type wall functions). The building surfaces are assumed smooth ($k_s = 0$ m). Concerning the ground surface, the use of such k_s -type wall functions can yield difficulties in simulating a horizontally homogeneous ABL, which is required in the upstream part of the computational domain because the “incident” wind tunnel profiles are used as inlet conditions. These inlet profiles should be the same as the “CFD incident profiles”, i.e. the profiles that would be obtained in an empty computational domain at the location where the building(s) would be positioned. This requirement is referred to as horizontal homogeneity. It refers to the absence of streamwise gradients in the vertical profiles of mean wind

speed and turbulence quantities (Richards and Hoxey 1993, Blocken et al. 2007a, 2007b, Franke et al. 2007, Yang et al. 2008, 2009, Gorlé et al. 2009). Due to the inconsistency between the turbulence model, wall function roughness modifications, inlet profiles and near-wall grid resolution, it is generally not possible to avoid such streamwise gradients (Blocken et al. 2007a). For CFD simulations of a horizontally homogeneous ABL with k_s -type wall functions, the appropriate relationship between k_s , y_0 and the roughness constant C_s should be satisfied. For Fluent 6 (up to at least version 6.3), this relationship was derived by Blocken et al. (2007a) (Eq. 2) and is used in this study.

$$k_s = \frac{9.793 y_0}{C_s} \quad (2)$$

4.4. Numerical simulations: results and validation

All simulations were performed with steady RANS which does not allow reproducing vortex shedding and will yield less good predictions in the wake (Murakami 1993, Tominaga et al. 2008b). However, in the present study, this part of the flow field is of lesser importance. Instead, the focus is on that part of the flow field through which the raindrops travel before impinging on the building facades. From the four RANS turbulence models tested, the RSM has the best potential to reproduce this flow pattern, because it allows taking turbulence anisotropy into account.

Fig. 4 compares the RSM simulation results with the PIV measurements in the low-rise building centreplane. A good agreement is obtained. The location and extent of the standing vortex and the absence of reattachment on the roof are well predicted. Note that the colour scales of the two figures are different, which does not allow a quantitative comparison based on this graph. Fig. 4b also shows the 13 vertical lines, along which more detailed results are reported in Fig. 5. Fig. 5 indicates that the performance of all turbulence models is fairly good, although they all seem to underestimate the vertical velocities directly upstream of the building and around the roof edge. Fig. 6 compares RSM with PIV measurements for the high-rise building. The location and the size of the standing vortex, the stagnation region at the building facade, the extent of the separation region on the roof and the speed-up over the building are quite well predicted. Fig. 7a shows that the standard k - ϵ model significantly underestimates the negative velocities in the standing vortex, while the RSM shows the best performance. All models show some underestimation of the positive velocities in the standing vortex. Fig. 7b also indicates the better performance of the RSM. Fig. 8 compares RSM and PIV in the centreplane of the two-building configuration. The location and size of the standing vortex between the buildings is well predicted, as are the extent of the separation region on the roof of both buildings, the stagnation region at the high-rise building facade and the speed-up over the high-rise building. Fig. 9 shows the deficiencies of the standard and realizable k - ϵ model in reproducing the strength of the standing vortex. Good results are obtained by the RNG k - ϵ model and RSM, although the former seems to slightly overestimate vortex strength. Based on these validation results, steady RANS with RSM is selected for the rest of the study.

5. Model application, results and discussion

5.1. Model application

3D steady RANS simulations with RSM are performed for the three building configurations. As opposed to the simulations in the previous section, this time the simulations are made at full scale, because raindrops will be injected in these flow patterns. Full-scale simulations avoid the need for scaling of raindrop sizes and raindrop-size distributions. The simulation characteristics and settings are as much as possible equal to those mentioned in section 4.3. Some particular differences are mentioned. The computational domain is taken twice as long, and the building(s) is/are positioned in the centre of the domain. The reason is that a sufficiently long upstream distance is needed because the raindrops have to be injected upstream of the building and outside the wind-flow pattern that is disturbed by the building. Because of the long upstream distance, horizontal inhomogeneity problems can be more pronounced (Blocken et al. 2007a). They are avoided in this study by applying the inlet profiles by Richards and Hoxey (1993) in combination with the standard wall functions by Launder and Spalding (1974), the roughness modification of these wall functions by Cebeci and Bradshaw (1977) and the sand-grain roughness height and roughness constant according to Eq. (2). The inlet mean wind speed profile is a logarithmic law with $y_0 = 0.03$ m, representing a grass-covered terrain without other obstacles (Wieringa 1992). The reference wind speed $U_{10} = 10$ m/s. Turbulent kinetic energy is calculated with $k = u^{*2}/C_\mu^{0.5}$ with $u^* = 0.69$ m/s and $C_\mu = 0.09$.

The calculation of the raindrop trajectories, the specific catch ratio and the catch ratio are performed with author-written program codes. The characteristics and settings of these simulations are similar to those in

(Blocken and Carmeliet 2006). Calculations of the raindrop motions are conducted in the flow patterns with $U_{10} = 10$ m/s for a range of raindrop diameters: from 0.5 to 1.0 mm in steps of 0.1 mm, from 1.0 mm to 2.0 mm in steps of 0.2 mm and from 2.0 mm to 6.0 mm in steps of 1.0 mm. Note that the calculations of the wind-flow pattern and the raindrop motions are decoupled, i.e. raindrop motions are calculated based on the mean wind-flow pattern, but no influence of raindrop motion on the mean wind-flow pattern is considered. For each position at the building facade (full-scale resolution 0.05×0.05 m²) and for each raindrop diameter, the specific catch ratio η_d is determined. Next, the catch ratio η is determined from the specific catch ratio and the horizontal raindrop-size distribution $f_h(d)$ (Fig. 10) for two horizontal rainfall intensities: $R_h = 5$ mm/h and $R_h = 30$ mm/h. The size distribution $f_h(d)$ is calculated from the size distribution $f(d)$ in a volume of air (Best 1950). The conversion from $f(d)$ to $f_h(d)$ is performed using the raindrop terminal velocity of fall (see Blocken and Carmeliet 2004).

5.2. Results

The mutual influence of the two buildings on their WDR exposure is analysed by comparing the results for the two-building configuration with those for the isolated buildings.

Fig. 11 displays contours of the catch ratio on the front facade of the isolated low-rise building, without and with the presence of the high-rise building, for $R_h = 5$ mm/h. The presence of the high-rise building significantly decreases the WDR exposure at the low-rise building facade. The maximum value decreases by 23% from 1.60 to 1.23. Fig. 12 shows that this effect is equally pronounced for $R_h = 30$ mm/h.

Fig. 13 shows catch ratio contours on the front facade of the high-rise building, without and with the low-rise building present, for $R_h = 5$ mm/h. The presence of the low-rise building increases the WDR exposure of the lower part of the high-rise building facade, while the WDR of the upper part does not change significantly. The catch ratio at the side edges increases by about a factor 2 compared to the situation without low-rise building present. More towards the middle of the lower part of the facade, the catch ratio increases by even more than a factor 2. Fig. 14 shows that this effect is almost equally pronounced for $R_h = 30$ mm/h.

5.3. Discussion

The influence of the high-rise building on the WDR exposure of the low-rise building can be explained based on the wind-blocking effect, which was investigated earlier for the case of WDR on isolated buildings (Blocken and Carmeliet 2006). The wind-blocking effect refers to the disturbance of the wind-flow pattern by the presence of the building. In particular for WDR, the decrease of the streamwise horizontal wind-velocity component upstream of the building (wind-speed slow-down) is important, as this component carries the rain to the facade. Fig. 15 compares contours of the dimensionless streamwise velocity component U/U_{10} in the centreplane of the three building configurations. Isolines are displayed to indicate the extent of the wind-blocking effect. Comparing Fig. 15a and c shows that the horizontal wind velocity component upstream and above the low-rise building is significantly decreased by the presence of the high-rise building. The raindrops that will hit the low-rise building facade and that travel through this region will therefore receive less momentum by the wind, resulting in lower catch ratios. Fig. 16 demonstrates this by displaying trajectories of 2 mm raindrops that are released from a horizontal line in the centreplane of the building(s). In both Fig. 16a and b, the low-rise building is at the same position and the drops are also released from the same positions. Note that 2 mm raindrops represent an important fraction of rainfall with $R_h = 5$ and 30 mm/h (Fig. 10). In Fig. 16a, the raindrops approaching the low-rise building have a larger horizontal velocity component and travel further than in Fig. 16b. This case shows the importance of the “upstream disturbance” caused by buildings, i.e. the disturbance that is caused by buildings because they influence the wind-flow pattern upstream of their position.

The influence of the low-rise building on the high-rise building is due to the increased strength of the standing vortex because it is confined in the passage between the two buildings. This increased strength can be observed by comparing Fig. 6 with Fig. 8, and Fig. 7 with Fig. 9. Fig. 13d and 14d particularly show a high catch ratio at the lower part of the side edges. The reason for this is the structure of the standing vortex in this region, that sweeps around these building edges. Fig. 17 shows that the streamwise component of the velocity vector is significantly more pronounced near the side edges, providing more streamwise momentum to the rain. This effect, together with the confined vortex, yields the local high catch ratio. Fig. 18 presents raindrop trajectories of 2 mm drops, released from either a horizontal line in the vertical centreplane ($z = 25$ m) or from a horizontal line that is shifted 20 m in the positive z -direction. In Fig. 18c, the trajectories near the lower part of the side edges are swept away from the corner, while in Fig. 18d, the higher streamwise velocity components near those edges cause the same raindrops to hit the facade near these edges. Fig. 19 provides more information on the vortex structure by displaying velocity vectors in two horizontal planes, one at mid-height of the low-rise building and one at the height of this building. At both altitudes, a strong outward flow is observed at the edges of the high-rise building, which is responsible for sweeping the raindrops towards these edges. This is confirmed

by Fig. 20 that shows the outward movement of the raindrops towards the building edges. While one might generally expect that the effect of an upstream building is to provide shelter to its downstream neighbour, this case shows that this is not necessarily true, and that the “downstream disturbance” caused by a building can also increase, rather than decrease, the WDR exposure.

6. Comments on the European Standard Draft obstruction factor

The European Standard Draft (ESD) prEN ISO 15927-3 “Hygrothermal performance of buildings - Calculation and presentation of climatic data - Part 3: Calculation of a driving rain index for vertical surfaces from hourly wind and rain data (ISO/DIS 15927-3:2006)” provides two procedures to calculate the amount of WDR impinging on building facades (CEN 2006). In those procedures, correction factors are used to convert “airfield” WDR amounts to WDR amounts to be expected on building facades. One of these factors is the obstruction factor “O”. It is defined as the “*factor which relates to shelter from the very local environment, and allows for obstructions such as buildings, fences and trees close to and upwind of the wall*”. The ESD mentions that the obstruction of a certain facade should be assessed by determining the horizontal distance to the nearest obstacle, which is at least as high as this facade or wall, along the “line of sight from the wall”. The line of sight is defined as “*the horizontal view away from the wall, over a sector spanning about 25° either side of the normal to the wall*”. The factor can then be determined from Table 1. The obstruction factor only applies to downstream disturbances, and it assumes that – at most – no reduction of the WDR exposure is provided. The present study however has shown that upstream buildings can also *increase* the WDR exposure of their downstream neighbours, and that downstream buildings can also have an important effect on buildings located upstream. The concept of the obstruction factor appears too simple to take into account the complex mutual influence of buildings on their WDR exposure. Care is therefore needed when applying this factor. While it can be rightfully criticised, it should also be noted that, given the complexity of building aerodynamics and WDR, the ESD is already a very valuable contribution that can be used for practical WDR assessment when time-consuming wind tunnel experiments or CFD simulations are not an option.

7. Discussion

The CFD simulations of the wind-flow pattern have only been validated in the centreplane of the building(s). While a complete validation study should also include detailed comparisons with experiments outside this plane, the present validation study was found useful to discriminate between the four different turbulence models and to justify the selection of the RSM for further simulations.

Turbulent dispersion of raindrops has been neglected. While this is considered valid for low-rise buildings and the upper part of high-rise buildings, it could be important for the lower part of high-rise buildings, where the simulated mean raindrop trajectories are almost parallel to the facade and often do not hit the facade (see Figs. 16b and 18). In this case, small turbulent deviations from the mean trajectory might cause the raindrops to hit the facade anyway. This effect might increase the catch ratio at the lower part of the facade, but this does not compromise the observations concerning the mutual influence of buildings on their WDR exposure in this paper.

Future work should include modelling the turbulent dispersion of WDR. This will however require some modifications in the modelling procedure. The procedure used in this paper employs the “steady stream tube” approach, as explained in section 3. It requires only three raindrop trajectories (i.e. a stream tube) to be computed to calculate the specific catch ratio at a given facade position. Including turbulent dispersion of raindrops implies that steady-state stream tubes for raindrops can no longer be defined, and that the specific catch ratio can no longer be calculated this way. Instead, calculating the specific catch ratio at a given position will therefore have to be performed by counting the number of raindrop trajectories ending at this position. This will require a much larger amount of raindrop trajectories to be computed, to achieve results that are independent of the number of injected raindrops. In addition, accurately modelling turbulent dispersion requires accurate information on the turbulence field. Given the deficiencies of the $k-\epsilon$ family of turbulence models, RSM but possibly DES/LES will be required. The problem is that the “steady stream tube” approach is already a very time-consuming procedure, because Lagrangian particle tracking has to be performed for all 15 raindrop diameters, and this should be repeated for every reference wind speed and every reference wind direction. Adding turbulent dispersion and maybe resorting to transient wind-flow pattern calculations with DES/LES will drastically increase computation times. The Lagrangian approach is the natural approach for dealing with particle motion. As an alternative to Lagrangian particle tracking, however, Eulerian particle dispersion could be applied (Shirolkar et al. 1996, Loth 2000). The Eulerian description applied to the rain phase assumes that the characteristics of the raindrops can be described as a continuum. This assumption allows the rain phase to be treated with the same discretisation and numerical techniques as used for the continuous (air) phase. While this can significantly reduce the computational cost, the description of turbulent diffusion is, however, more straightforward with the Lagrangian approach (Loth 2000).

The validation study for the mean wind-flow pattern showed that RSM outperformed the $k-\epsilon$ models. The raindrop trajectories are calculated based on the mean wind-flow pattern, but because of raindrop inertia, the catch ratio results can be expected to be less influenced by turbulence model deficiencies than the mean wind-flow pattern itself. Future research could focus on the actual differences in catch ratio results obtained by different turbulence models. Also this type of sensitivity studies would strongly benefit from a less computationally expensive procedure for WDR simulations.

This study has been limited to only one particular building configuration of only two buildings and to only one reference wind speed and one reference wind direction. Its intention has only been to be a first step and to indicate the importance of the mutual influence and some shortcomings of the ESD obstruction factor. Future research should focus on different reference wind speed and different reference wind directions for the same building configuration. Future research should also consider other building configurations, including different separation distances for the present two-building configuration. Other configurations also include a high-rise building upstream of a low-rise building. In this case, the high-rise building is expected to provide shelter to the low-rise building, depending on the distance between both buildings. Analysing the mutual influence for this configuration however is more complex, because the wake effects by the high-rise building might be dominant, and steady RANS is generally unsuitable for such cases. Instead, DES and/or LES should be used.

8. Conclusions

Wind-driven rain (WDR) deposition on a two-building configuration, consisting of a high-rise building screened by a low-rise building, has been studied with Computational Fluid Dynamics (CFD). The goal was to analyse the mutual influence of the two buildings on their WDR exposure, and to relate the findings to the European Standard Draft (ESD) obstruction factor. The following conclusions are made:

- Validation with PIV wind tunnel measurements has shown that the Reynolds stress model considerably outperforms the standard and realizable $k-\epsilon$ model for mean wind speed predictions in the upstream part of the domain. The better performance was most pronounced concerning the strength of the standing vortex in the passage between the two buildings. This is considered very important, because this standing vortex is one of the main features governing the WDR deposition in the two-building configuration.
- For the case studied here, two types of mutual influence can be distinguished: upstream disturbance and downstream disturbance. The first refers to the influence of a downstream building on its upstream neighbour, due to the upstream disturbance of the wind by a building. The second refers to the influence of an upstream building on its downstream neighbour. For the case studied here, with a reference wind speed $U_{10} = 10$ m/s and wind direction perpendicular to the facades, the mutual influence of both buildings on each other's WDR exposure was very pronounced and to some extent opposite to what might be expected:
 - (1) The low-rise building does not partly shield the high-rise building from wind and WDR. Instead, it provides higher WDR exposure by increasing the strength of the standing vortex ("downstream disturbance"). This locally increases WDR intensities on the high-rise building facade by more than a factor 2 for both $R_h = 5$ and 30 mm/h.
 - (2) The high-rise building influences deposition on the low-rise building facade ("upstream disturbance"): the wind-blocking effect by the high-rise building yields a reduction in WDR deposition on the low-rise building facade by about 25% for both $R_h = 5$ and 30 mm/h.
- In the ESD for WDR assessment, the mutual influence of buildings can only be taken into account by a simplified reduction factor, called the obstruction factor. It only considers downstream disturbances, and does not consider the possibility of increased WDR exposure due to the mutual influence. Care should be exercised when calculating WDR using the current version of the obstruction factor.

Acknowledgements

The authors want to express their gratitude to Mark Broers, Heleen Claes and Carlos Rodrigues for their assistance during the course of this research work. We also thank the anonymous reviewers for their valuable comments.

Nomenclature

B_1, L_1, H_1	width, length, height of the low-rise building (m)
B_2, L_2, H_2	width, length, height of the high-rise building (m)
$C_{1\epsilon}, C_{2\epsilon}$	turbulence model constants (-)
C_μ	turbulence model constant, variable in realizable $k-\epsilon$ model
$C_{1PS}, C_{2PS}, C_{1'PS}, C_{2'PS}$	turbulence model constants – linear pressure strain model
C_s	roughness constant in the standard wall function modified-for-roughness (-)

d	raindrop diameter (mm)
f(d)	probability-density function of raindrop size in a volume of air (m^{-1})
$f_h(d)$	probability-density function of raindrop size falling through a horizontal plane (m^{-1})
k	turbulent kinetic energy (m^2s^{-2})
k_s	equivalent sand-grain roughness height (m)
Re	Reynolds number (-)
R_h	horizontal rainfall intensity, i.e. through a horizontal plane ($Lm^{-2}h^{-1}$ or mmh^{-1})
R_{wdr}	wind-driven rain intensity ($Lm^{-2}h^{-1}$ or mmh^{-1})
t	time (s)
u^*	friction velocity associated with the inlet profiles of U, k and ϵ (ms^{-1})
U	streamwise horizontal component of the mean wind-velocity vector (ms^{-1})
U_{10}	reference wind speed at 10 m height in the upstream undisturbed flow (ms^{-1})
U_{ref}	reference wind speed at $y/H_2 = 1.5$ (ms^{-1})
V	vertical component of the mean wind-velocity vector (ms^{-1})
x, z	streamwise and spanwise co-ordinate (m)
y	vertical co-ordinate (m)
y_0	aerodynamic roughness length (m)
Δt	time delay between two laser pulses (s)
ϵ	turbulence dissipation rate (m^2s^{-3})
η_d	specific catch ratio (-)
η	catch ratio (-)
κ	von Karman constant (≈ 0.42)
$\sigma_k, \sigma_\epsilon$	turbulent Prandtl numbers for k and ϵ (-)
σ_v, σ_w	standard deviation of turbulent fluctuations in vertical and lateral direction (m/s)
ϕ_{10}	wind direction at 10 m height in the upstream undisturbed flow (degrees from north)
CFD	Computational Fluid Dynamics
ESD	European Standard Draft
RANS	Reynolds-Averaged Navier-Stokes
WDR	Wind-Driven Rain

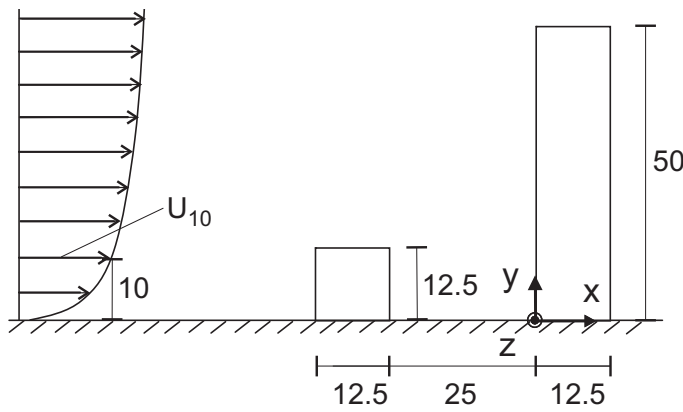
References

- Abuku, M., Blocken, B., Nore, K., Thue, J.V., Carmeliet, J., Roels, S., 2009. On the validity of numerical wind-driven rain simulation on a rectangular low-rise building under various oblique winds. *Building and Environment* 44(3) 621– 632.
- Best, A.C., 1950. The size distribution of raindrops. *Quarterly Journal of the Royal Meteorological Society* 76: 16-36.
- Blocken, B., Carmeliet, J., 2002. Spatial and temporal distribution of driving rain on a low-rise building. *Wind and Structures* 5, 5, 441-462.
- Blocken, B., Carmeliet, J., 2004. A review on wind-driven rain research in building science. *Journal of Wind Engineering and Industrial Aerodynamics* 92, 13, 1079-1130.
- Blocken, B., Carmeliet, J., 2005. High-resolution wind-driven rain measurements on a low-rise building – experimental data for model development and model validation. *Journal of Wind Engineering and Industrial Aerodynamics*, 93, 12, 905-928.
- Blocken, B., Carmeliet, J., 2006. The influence of the wind-blocking effect by a building on its wind-driven rain exposure. *Journal of Wind Engineering and Industrial Aerodynamics* 94(2), 101-127.
- Blocken, B., Carmeliet J., 2007a. On the errors associated with the use of hourly data in wind-driven rain calculations on building facades. *Atmospheric Environment* 41(11), 2335-2343.
- Blocken B, Carmeliet J. 2007b. Validation of CFD simulations of wind-driven rain on a low-rise building facade. *Building and Environment* 42(7): 2530–2548.
- Blocken, B., Stathopoulos, T., Carmeliet, J., 2007a. CFD simulation of the atmospheric boundary layer: wall function problems. *Atmospheric Environment* 41(2): 238-252.
- Blocken, B., Carmeliet, J., Stathopoulos, T., 2007b. CFD evaluation of wind speed conditions in passages between parallel buildings—effect of wall-function roughness modifications for the atmospheric boundary layer flow. *Journal of Wind Engineering and Industrial Aerodynamics* 95(9-11) 941-962.
- Briggen, P.M., Blocken, B., Schellen, H.L., 2009. Wind-driven rain on the facade of a monumental tower: numerical simulation, full-scale validation and sensitivity analysis. *Building and Environment* 44(8): 1675-1690.

- Cebeci, T., Bradshaw, P., 1977. Momentum transfer in boundary layers. Hemisphere Publishing Corporation, New York.
- CEN 2006. DRAFT prEN ISO 15927-3. Hygrothermal performance of buildings - Calculation and presentation of climatic data - Part 3: Calculation of a driving rain index for vertical surfaces from hourly wind and rain data (ISO/DIS 15927-3:2006).
- Choi, E.C.C., 1991. Numerical simulation of wind-driven rain falling onto a 2-D building, in: Asia Pacific Conf. on Computational Mechanics, Hong Kong, 1721-1728.
- Choi, E.C.C., 1993. Simulation of wind-driven rain around a building. *Journal of Wind Engineering and Industrial Aerodynamics* 46&47, 721-729.
- Choi, E.C.C., 1994. Determination of wind-driven rain intensity on building faces. *Journal of Wind Engineering and Industrial Aerodynamics* 51, 55-69.
- Choi, E.C.C., 1997. Numerical modeling of gust effect on wind-driven rain, *Journal of Wind Engineering and Industrial Aerodynamics* 72, 107-116.
- Dezsö-Weidinger, G., Stitou, A., van Beeck, J., Riethmuller, M.L., 2003. Measurement of the turbulent mass flux with PTV in a street canyon. *Journal of Wind Engineering and Industrial Aerodynamics* 91(9): 1117-1131.
- Fluent Inc., 2006. Fluent 6.3 user's guide, Lebanon.
- Franke, J., Hellsten, A., Schlünzen, H., Carissimo, B. 2007. Best practice guideline for the CFD simulation of flows in the urban environment. COST Action 732: Quality Assurance and Improvement of Microscale Meteorological Models.
- Gibson, M.M., Launder, B.E., 1978. Ground effects on pressure fluctuations in the Atmospheric Boundary Layer. *Journal of Fluid Mechanics* 86, 491-511.
- Gorlé, C., van Beeck, J., Rambaud, P., Van Tendeloo, G., 2008. CFD modelling of small particle dispersion: the influence of the turbulence kinetic energy in the atmospheric boundary layer. *Atmospheric Environment*. 43(3) 673-681.
- Hangan, H., 1999. Wind-driven rain studies. A C-FD-E approach. *Journal of Wind Engineering and Industrial Aerodynamics* 81, 323-331.
- Inculet, D., Surry, D., 1994. Simulation of wind-driven rain and wetting patterns on buildings. BLWTL-SS30-1994. Final report.
- Inculet, D.R., 2001. The design of cladding against wind-driven rain. Ph.D. thesis, The University of Western Ontario, London, Ontario, Canada, 297 p.
- Jones, W.P., Launder, B.E., 1972. The prediction of laminarization with a 2-equation model of turbulence. *International Journal of Heat and Mass Transfer* 15, 301.
- Karagiozis, A., Hadjisophocleous, G., Cao, S., 1997. Wind-driven rain distributions on two buildings. *Journal of Wind Engineering and Industrial Aerodynamics* 67&68, 559-572.
- Launder, B.E., 1989. Second-moment closure and its use in modeling turbulent industrial flows. *International Journal for Numerical Methods in Fluids* 9, 963-985.
- Launder, B.E., Reece, G.J., Rodi, W., 1975. Progress in the development of a Reynolds-stress turbulence closure. *Journal of Fluid Mechanics* 86, 537-566.
- Launder, B.E., Spalding, D.B., 1974. The numerical computation of turbulent flows, *Computer Methods in Applied Mechanics and Engineering* 3, pp. 269-289.
- Loth, E., 2000. Numerical approaches for motion of dispersed particles, droplets, and bubbles. *Progress in Energy and Combustion Science* 26, 161-223.
- Murakami, S., 1993. Comparison of various turbulence models applied to a bluff body. *Journal of Wind Engineering and Industrial Aerodynamics* 46 & 47: 21-36.
- Nore, K., Blocken, B., Jelle, B.P., Thue, J.V., Carmeliet, J., 2007. A dataset of wind-driven rain measurements on a low-rise test building in Norway. *Building and Environment* 42(5): 2150-2165.
- Penwarden, A.D., Wise, A.F.E., 1975. Wind environment around buildings. Building Research Establishment Report, Department of Environment, BRE, HMSO, London, UK.
- Richards, P.J., Hoxey, R.P., 1993. Appropriate boundary conditions for computational wind engineering models using the k- ϵ turbulence model. *Journal of Wind Engineering and Industrial Aerodynamics* 46&47: 145-153.
- Sagrado, A.P.G., van Beeck, J., Rambaud, P., Olivari, D., 2002. Numerical and experimental modeling of pollutant dispersion in a street canyon. *Journal of Wind Engineering and Industrial Aerodynamics* 90(4-5), 321-339.
- Scarano, F., Riethmuller, M.L., 2000. Advances in iterative multigrid PIV image processing. *Experiments in Fluids Suppl. S* 29, S51-60.
- Sexton, D.E., 1968. Building aerodynamics. Current Paper 64/68, Building Research Station, also in: Proceedings of the CIB Symposium on Weathertight Joints for Walls, Oslo, September 25-28, 1967.
- Shih, T.H., Liou, W.W., Shabbir, A., Zhu, J., 1995. A new k- ϵ eddy-viscosity model for high Reynolds number turbulent flows – model development and validation. *Computers and Fluids* 24, 3, 227-238.

- Shirolkar, J.S., Coimbra, C.F.M., McQuay, M.Q., 1996. Fundamental aspects of modeling turbulent particle dispersion in dilute flows. *Progress in Energy and Combustion Science* 22, 363–399.
- Surry, D., Incelet, D.R., Skerlj, P.F., Lin, J-X., Davenport, A.G., 1994. Wind, rain and the building envelope: a status report of ongoing research at the University of Western Ontario. *Journal of Wind Engineering and Industrial Aerodynamics* 53, 19-36
- Tang, W., Davidson, C.I., Finger, S., Vance, K., 2004. Erosion of limestone building surfaces caused by wind-driven rain. 1. Field measurements. *Atmospheric Environment* 38, 33, 5589-5599.
- Tang, W., Davidson, C.I., 2004. Erosion of limestone building surfaces caused by wind-driven rain. 2. Numerical modelling. *Atmospheric Environment* 38, 33, 5601-5609.
- Tominaga, Y., Mochida, A., Yoshie, R., Kataoka, H., Nozu, T., Yoshikawa, M., Shirasawa, T. 2008a. AIJ guidelines for practical applications of CFD to pedestrian wind environment around buildings. *Journal of Wind Engineering and Industrial Aerodynamics* 96(10-11) 1749-1761.
- Tominaga, Y., Mochida, A., Murakami, S., Sawaki, S., 2008b. Comparison of various revised $k-\epsilon$ models and LES applied to flow around a high-rise building model with 1:1:2 shape placed within the surface boundary layer. *Journal of Wind Engineering and Industrial Aerodynamics* 96(4) 389-411.
- van Mook, F.J.R., 2002. Driving rain on building envelopes, Ph.D. thesis, Building Physics Group (FAGO), Eindhoven University of Technology, Eindhoven University Press, Eindhoven, The Netherlands, 198 p.
- Wieringa, J., 1992. Updating the Davenport roughness classification. *Journal of Wind Engineering and Industrial Aerodynamics* 41-44: 357-368.
- Wise, A.F.E., 1970. Wind effects due to groups of buildings, In: *Proceedings of the Royal Society Symposium Architectural Aerodynamics, Session 3, Effect of Buildings on the Local Wind*, London. pp. 26–27 February.
- Wise, A.F.E., Sexton, D.E., Lillywhite, M.S.T., 1965. Studies of air flow round buildings. *The Architects' Journal*, 141: (19th May), 1185–1189.
- Yakhot, V., Orszag, S. A., Thangam, S., Gatski, T. B. and Speziale, C. G., 1992. Development of turbulence models for shear flows by a double expansion technique, *Physics of Fluids A* 4 pp.1510-1520.
- Yang, W., Quan, Y., Jin, X., Tamura, Y. and Gu, M., 2008. Influences of equilibrium atmosphere boundary layer and turbulence parameters on wind load distributions of low-rise buildings. *Journal of Wind Engineering and Industrial Aerodynamics* 96(10-11): 2080-2092.
- Yang, Y., Gu, M., Chen, S., Jin, X., 2009. New inflow boundary conditions for modelling the neutral equilibrium atmospheric boundary layer in computational wind engineering. *Journal of Wind Engineering and Industrial Aerodynamics* 97(2) 88-95.

(a) side view



(b) front view

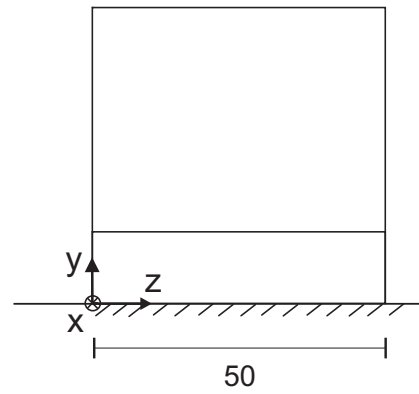


Fig. 1. Geometry of the two-building configuration: high-rise building screened by a low-rise building: (a) side view; (b) front view. Dimensions in m.

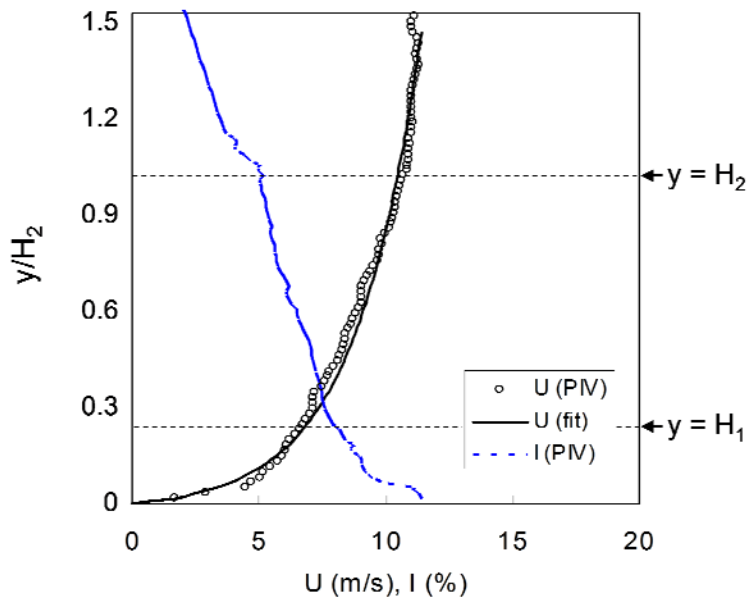


Fig. 2. Incident vertical profiles of mean wind speed U and turbulence intensity I obtained from the PIV measurements. The mean wind speed profile closely resembles a log law with $u^* = 1.1$ m/s and $y_0 = 0.00125$ m. H_1 and H_2 are the height of the low-rise and high-rise building, respectively.

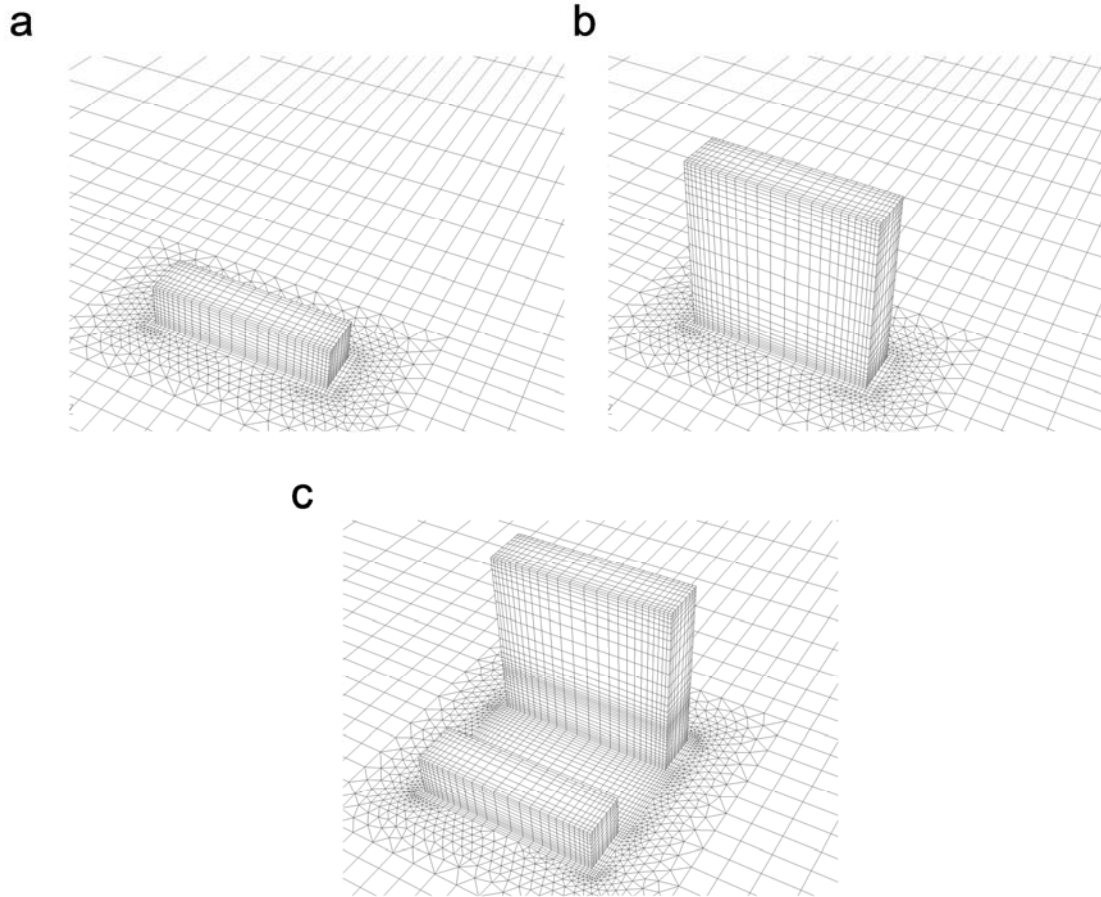


Fig. 3. Computational grids on the building surfaces and part of the ground surface for (a) low-rise building; (b) high-rise building; and (c) two-building configuration.

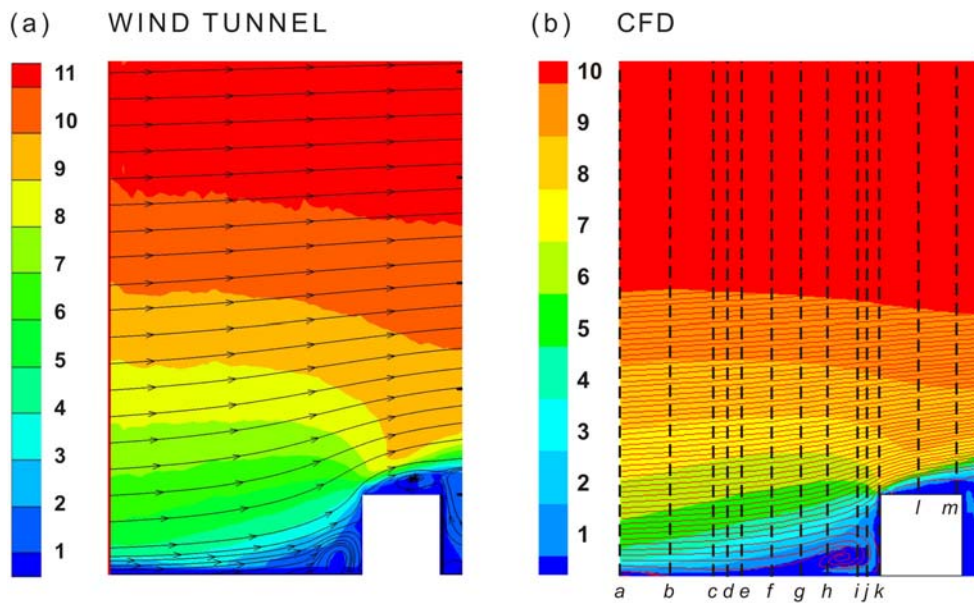


Fig. 4. Comparison between (a) wind tunnel and (b) CFD (RSM) results for mean wind speed in the low-rise building centreplane. Fig. 4b also indicates the vertical lines along which detailed comparisons are made in Fig. 5. Unit is m/s.

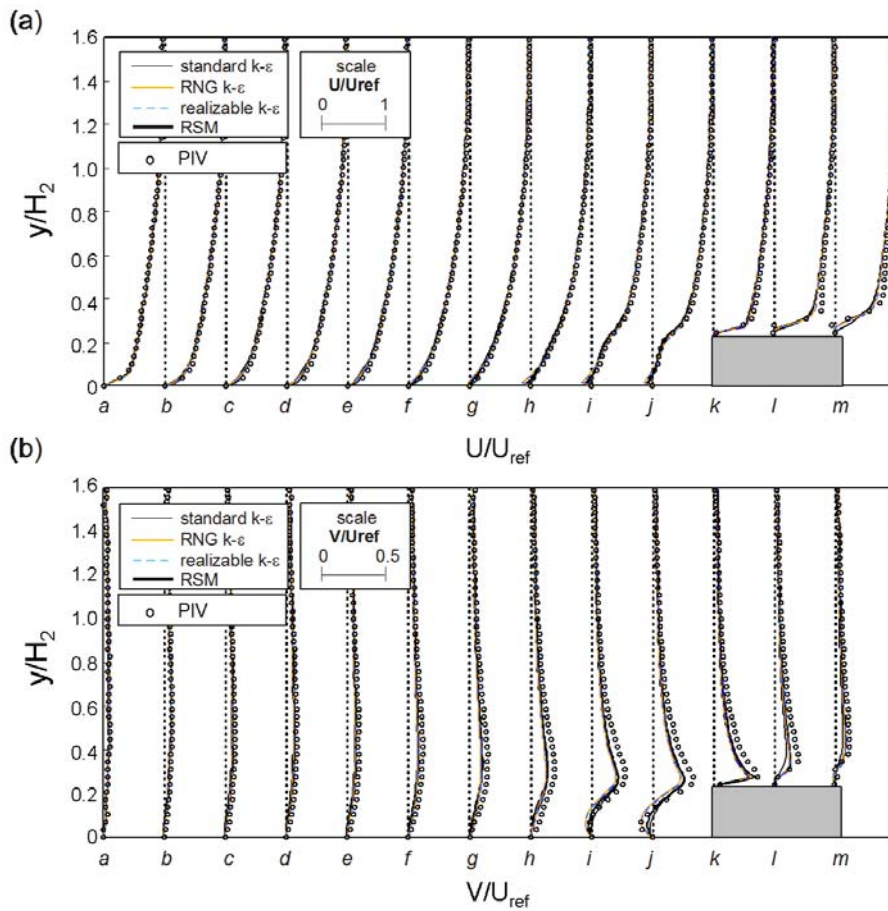


Fig. 5. Comparison between experiments and CFD results with four different turbulence models, along the vertical lines indicated in Fig. 4b. (a) Dimensionless streamwise velocity component; (b) dimensionless vertical velocity component. Note: building in image is not to scale.

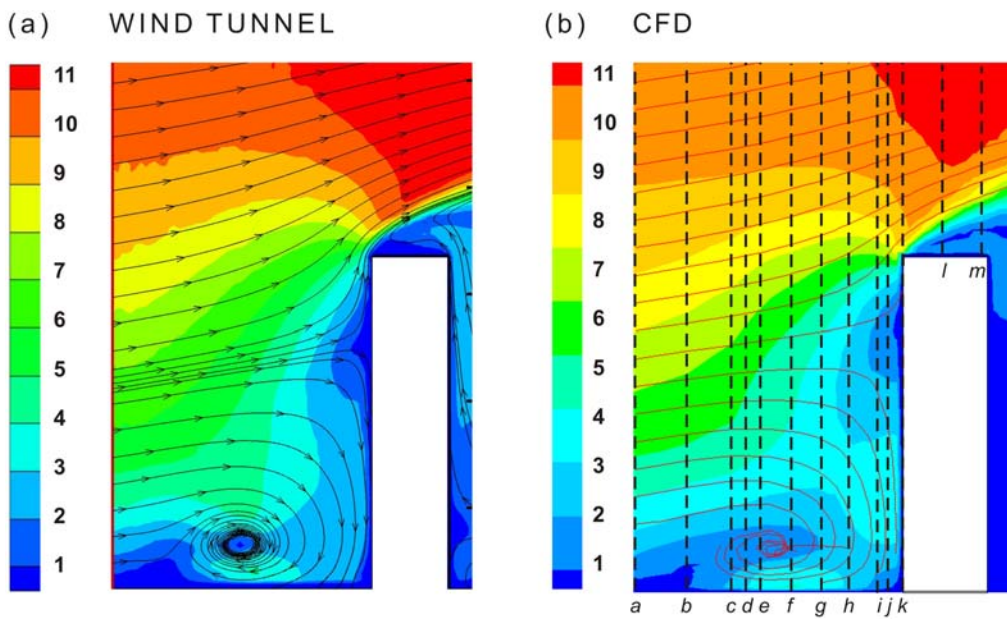


Fig. 6. Comparison between (a) wind tunnel and (b) CFD (RSM) results for mean wind speed in the high-rise building centreplane. Fig. 6b also indicates the vertical lines along which detailed comparisons are made in Fig. 7. Unit is m/s.

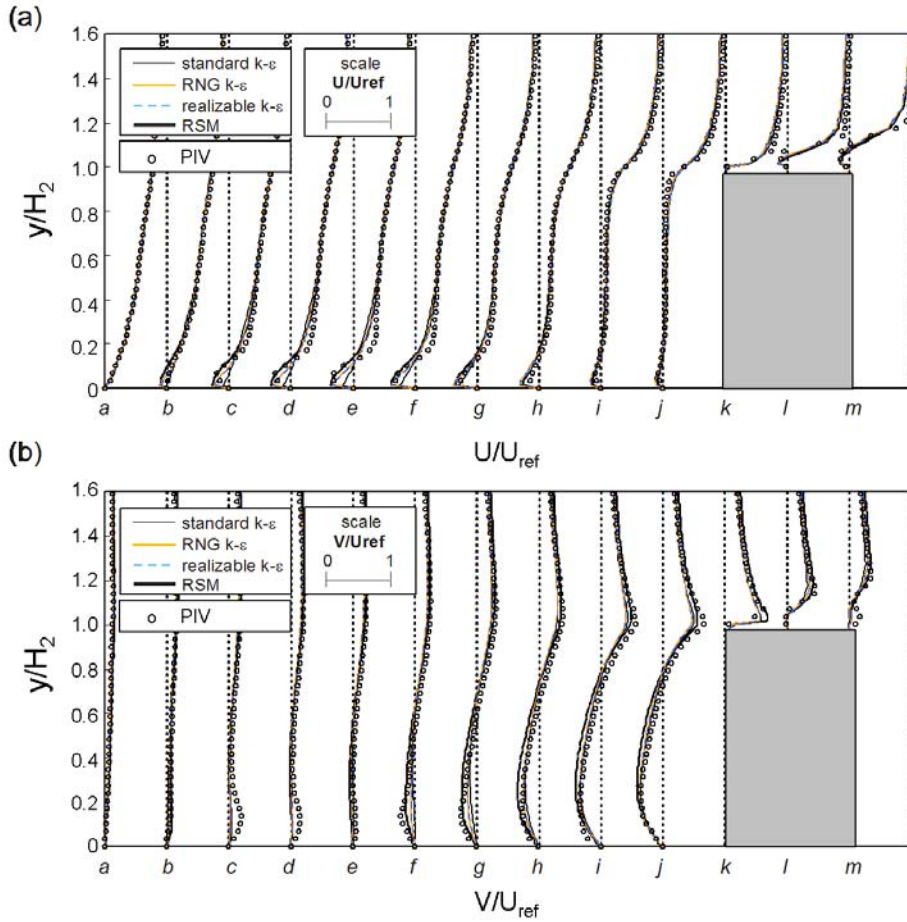


Fig. 7. Comparison between experiments and CFD results with four different turbulence models, along the vertical lines indicated in Fig. 6b. (a) Dimensionless streamwise velocity component; (b) dimensionless vertical velocity component. Note: building in image is not to scale.

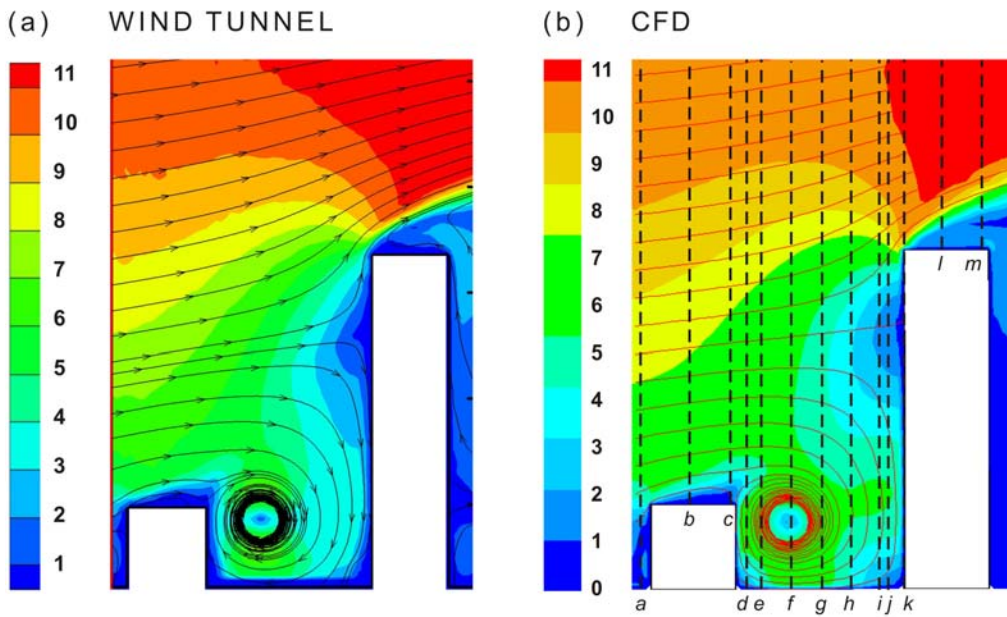


Fig. 8. Comparison between (a) wind tunnel and (b) CFD (RSM) results for mean wind speed in the centreplane of the two-building configuration. Fig. 8b also indicates the vertical lines along which detailed comparisons are made in Fig. 9. Unit is m/s.

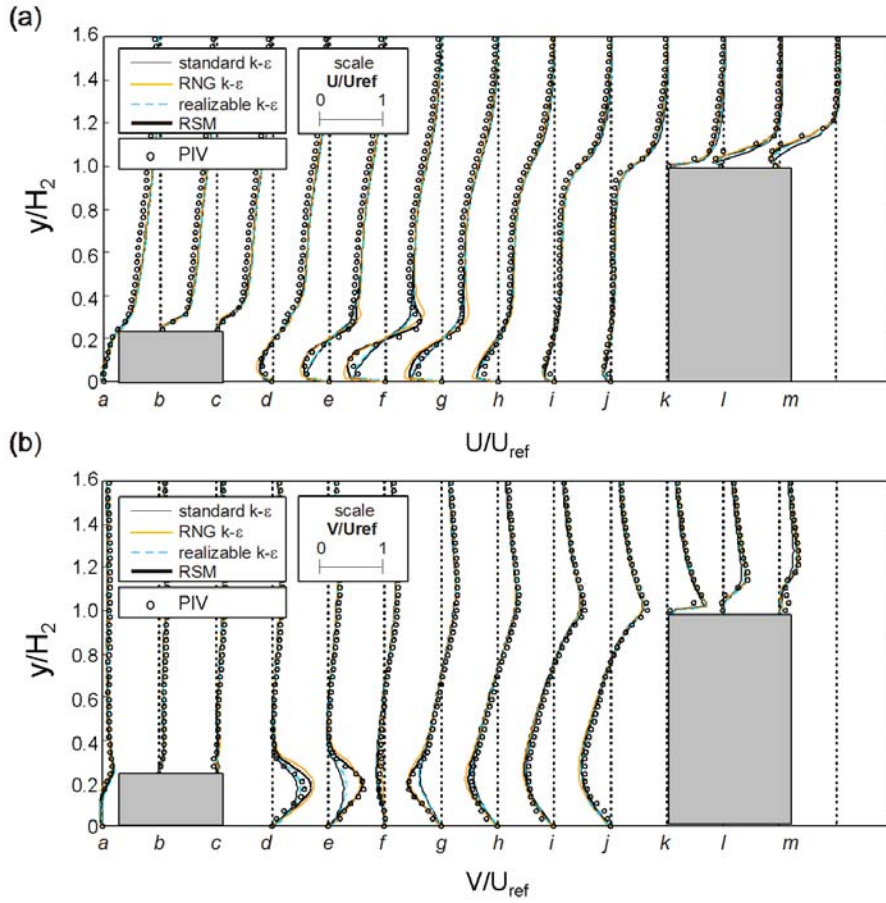


Fig. 9. Comparison between experiments and CFD results with four different turbulence models, along the vertical lines indicated in Fig. 8b. (a) Dimensionless streamwise velocity component; (b) dimensionless vertical velocity component. Note: buildings in image are not to scale.

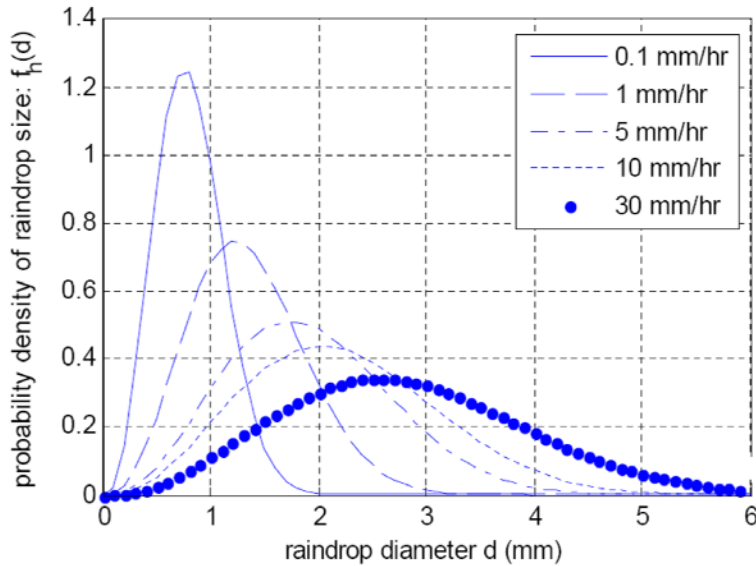


Fig. 10. Raindrop-size distribution $f_h(d)$ through a horizontal plane with the reference rainfall intensity R_h as a parameter – calculated from the raindrop-size distribution in the air according to Best (1950).

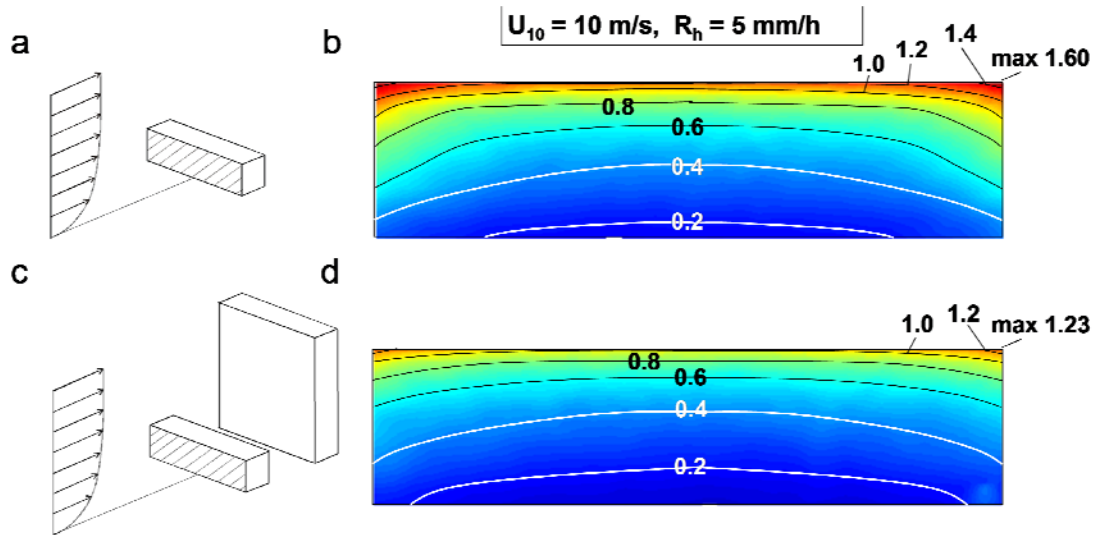


Fig. 11. (a-b) Catch ratio on the windward facade of the isolated low-rise building, for $U_{10} = 10 \text{ m/s}$ en $R_h = 5 \text{ mm/h}$; (c-d) Same, with high-rise building present.

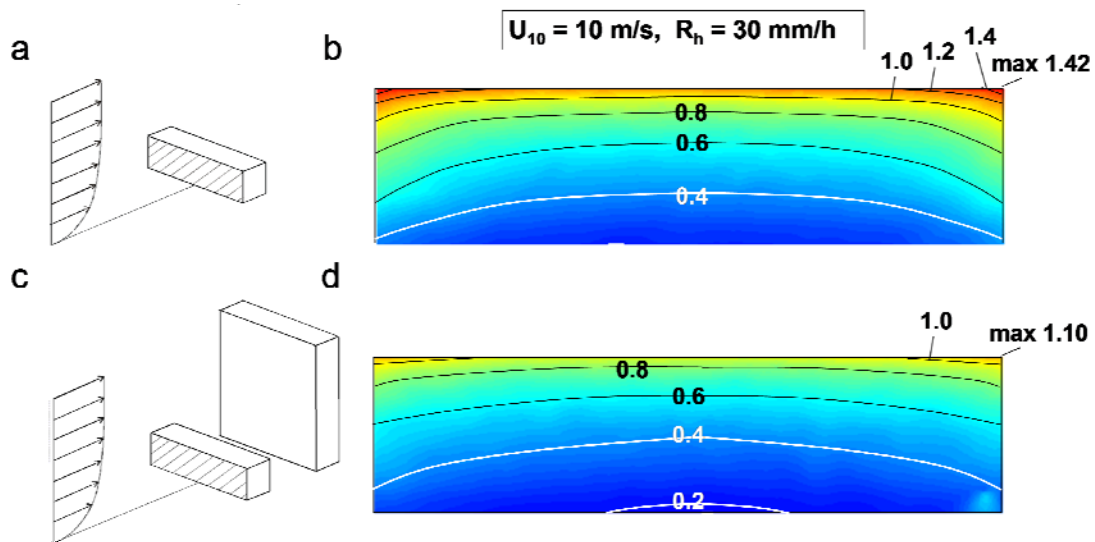


Fig. 12. (a-b) Catch ratio on the windward facade of the isolated low-rise building, for $U_{10} = 10 \text{ m/s}$ en $R_h = 30 \text{ mm/h}$; (c-d) Same, with high-rise building present.

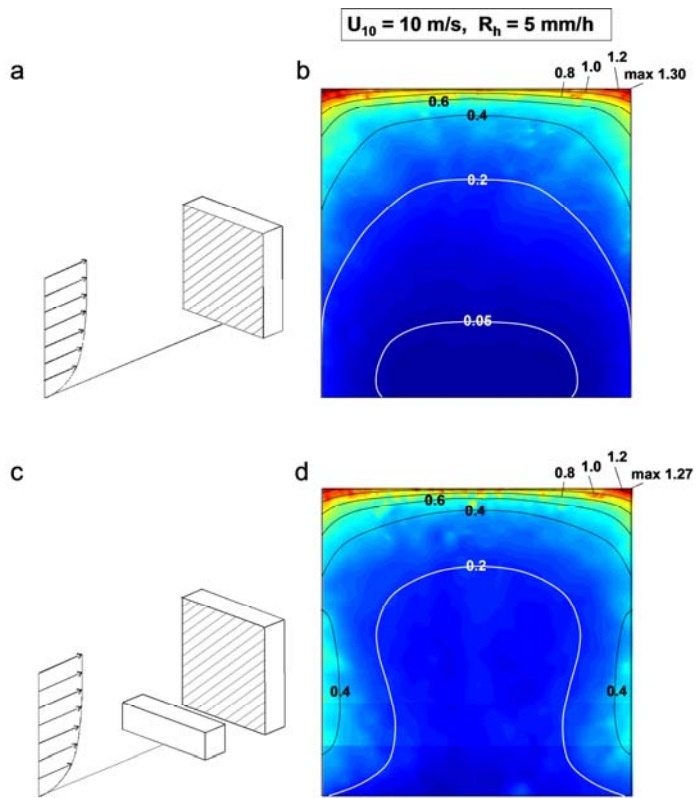


Fig. 13. (a-b) Catch ratio on the windward facade of the isolated high-rise building, for $U_{10} = 10 \text{ m/s}$ en $R_h = 5 \text{ mm/h}$; (c-d) Same, with low-rise building present.

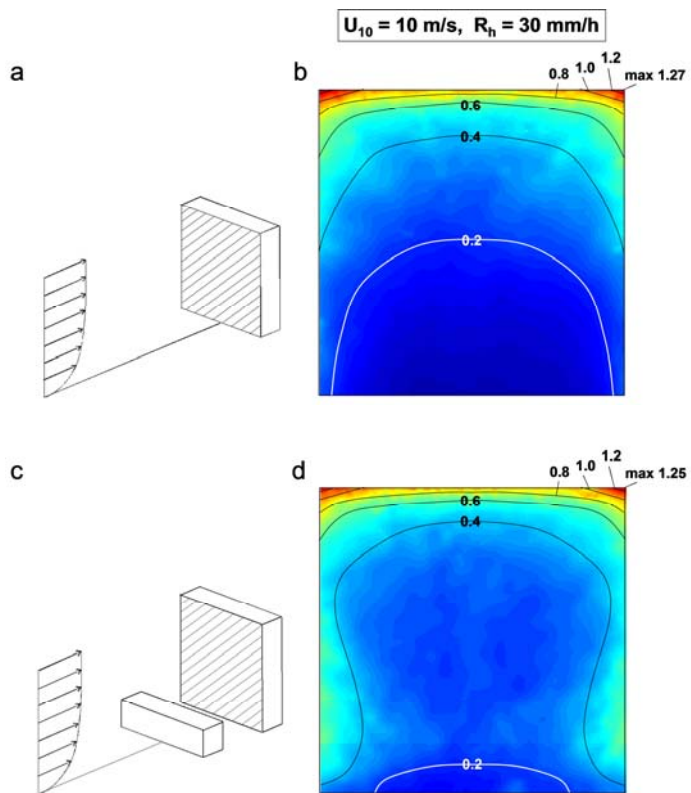


Fig. 14. (a-b) Catch ratio on the windward facade of the isolated high-rise building, for $U_{10} = 10 \text{ m/s}$ en $R_h = 30 \text{ mm/h}$; (c-d) Same, with low-rise building present.

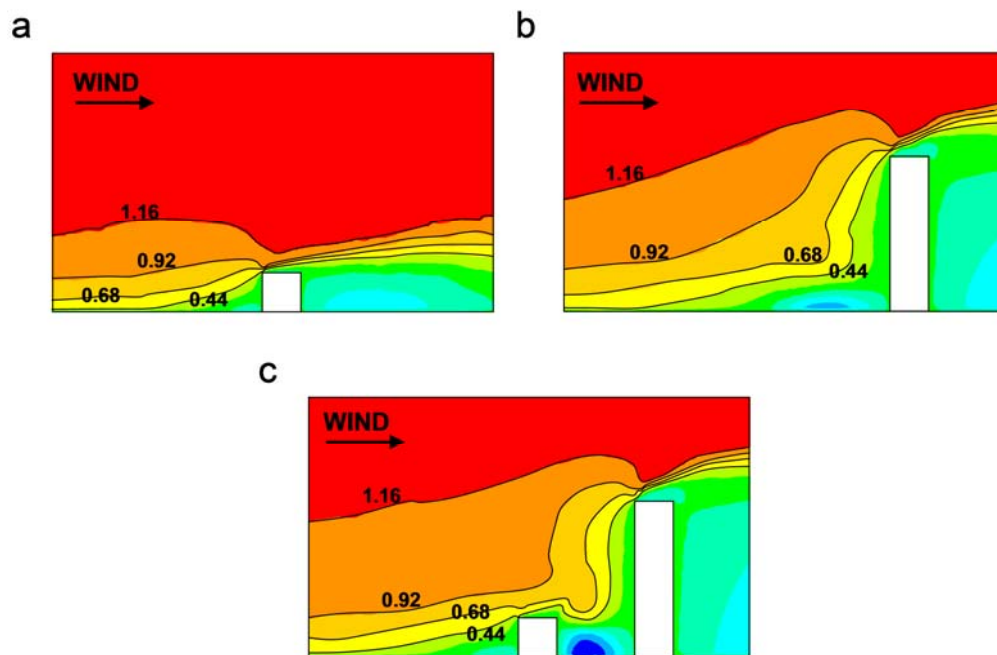


Fig. 15. Contours of streamwise velocity ratio U/U_{10} for (a) isolated low-rise building; (b) isolated high-rise building and (c) two-building configuration. The extent of the wind-blocking effect is demonstrated by the upward shifts in the upstream contour lines.

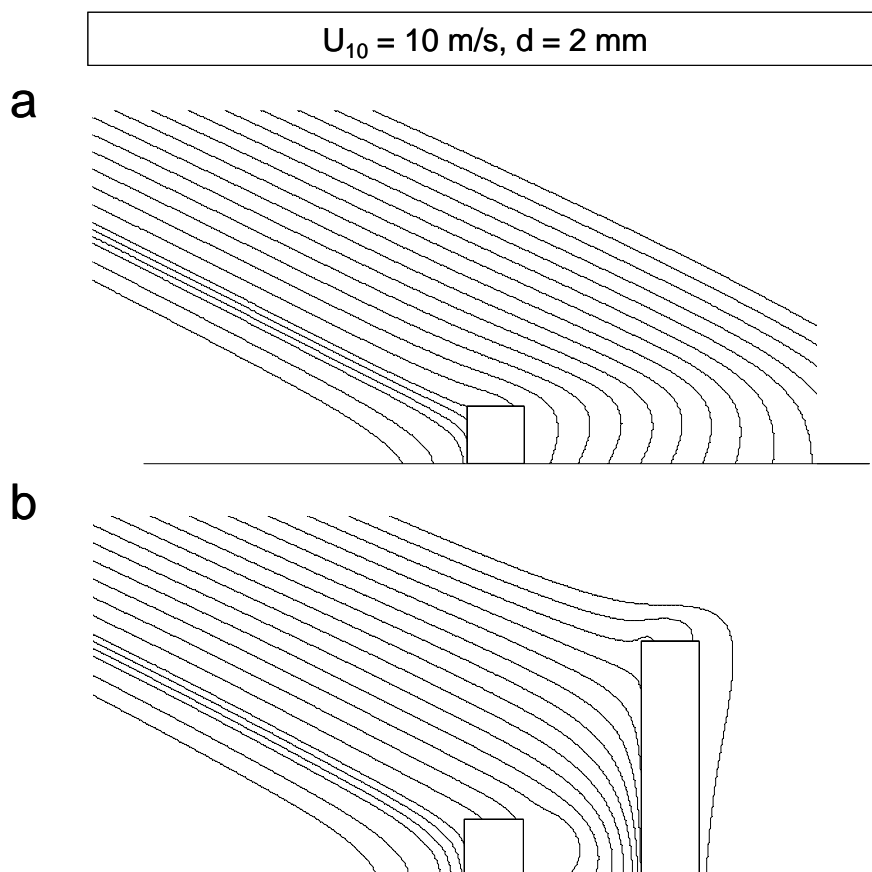


Fig. 16 Trajectories of 2 mm raindrops in the centreplane of the buildings in the $U_{10} = 10 \text{ m/s}$ wind-flow pattern. (a) For the isolated low-rise building; (b) for the two-building configuration.

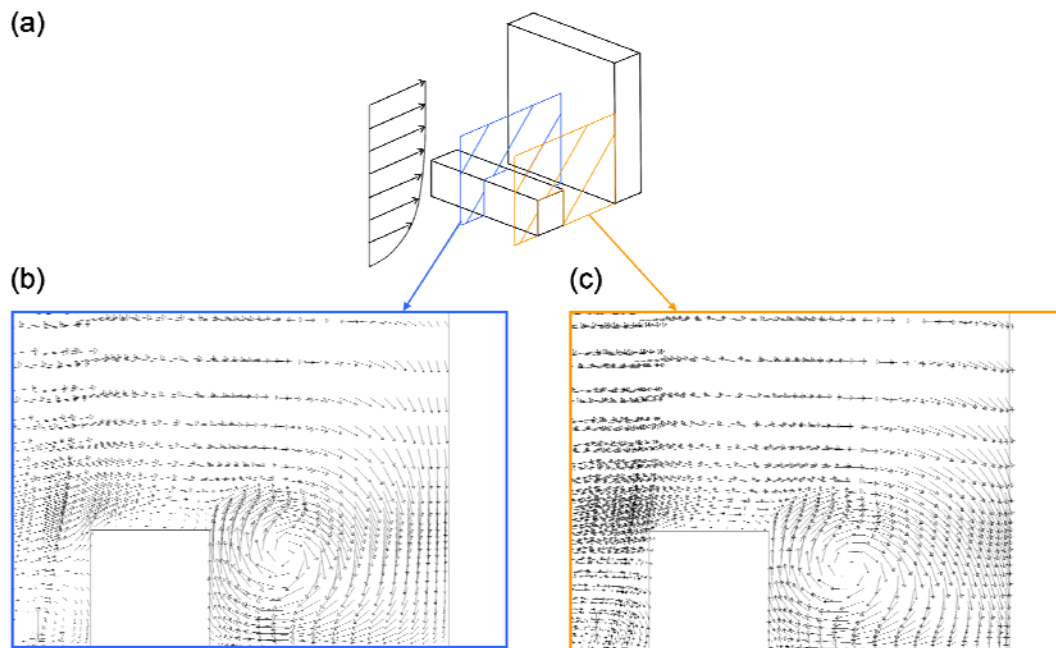


Fig. 17. Velocity vectors in two vertical planes indicating the vortex between the buildings.

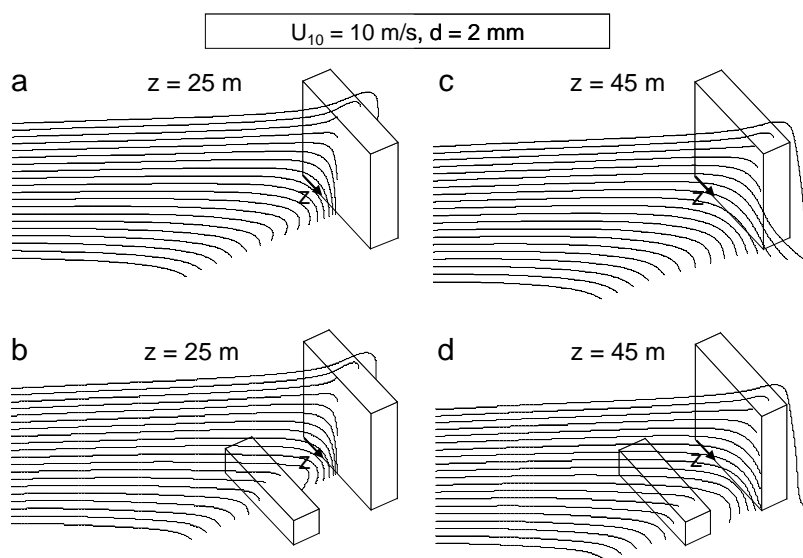


Fig. 18. Trajectories of 2 mm raindrops in the $U_{10} = 10$ m/s wind-flow pattern, for (a,c) isolated high-rise building and (b,d) two-building configuration. Drops are released from a horizontal line in (a,b) the vertical centreplane and (c,d) from a horizontal line in a vertical plane that is shifted 20 m from the centreplane.

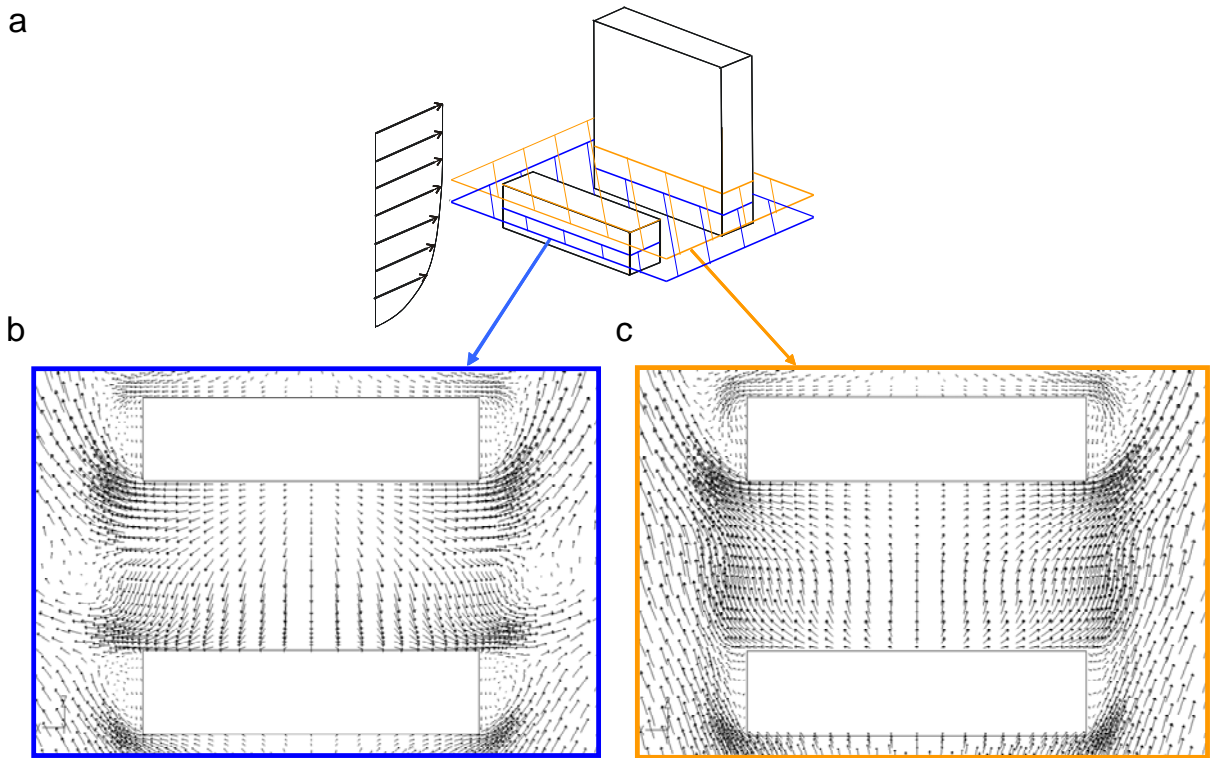


Fig. 19. Velocity vectors in two horizontal planes, one at mid-height and one at the height of the low-rise building. The vectors indicate the structure of the vortex between the buildings.

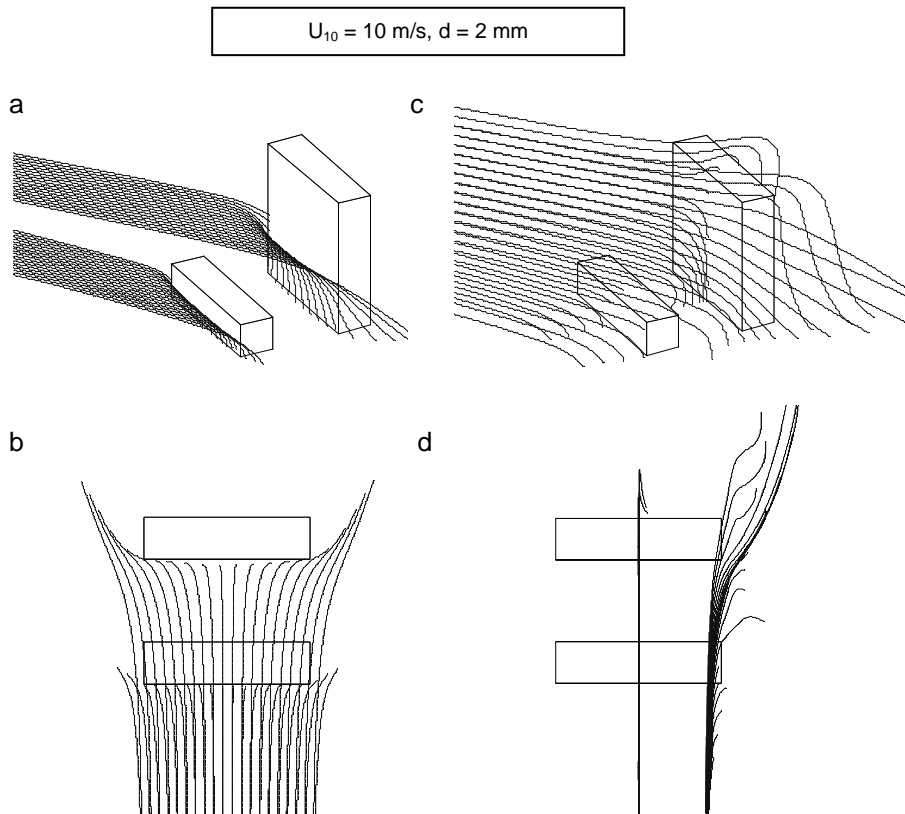


Fig. 20. Trajectories of 2 mm raindrops in the $U_{10} = 10 \text{ m/s}$ wind-flow pattern, for the two-building configuration. (a) Perspective and (b) plan view of drops released from a horizontal line in the vertical centreplane and from a horizontal line in a vertical plane that is shifted 20 m from the centreplane. (c-d) Same, but for drops released from two horizontal lines with a 60 m distance in between.